Journal of Quantitative Spectroscopy & Radiative Transfer 273 (2021) 107845

Contents lists available at ScienceDirect

Journal of Quantitative Spectroscopy & Radiative Transfer

journal homepage: www.elsevier.com/locate/jqsrt

Spectral degree of linear polarization and neutral points of polarization in snow and ice surfaces

Tomonori Tanikawa[a,*], Kazuhiko Masuda[a], Hiroshi Ishimoto[a], Teruo Aoki[b], Masahiro Hori[c], Masashi Niwano[a], Akihiro Hachikubo[d], Sumito Matoba[e], Konosuke Sugiura[c], Takenobu Toyota[e], Nozomu Ohkawara[a], Knut Stamnes[f]

[a] Meteorological Research Institute, Japan Meteorological Agency, Tsukuba, 305-0052, Japan
[b] National Institute of Polar Research, Tsukuba, 190-8518, Japan
[c] University of Toyama, Toyama, 930-8555, Japan
[d] Kitami Institute of Technology, Kitami, 090-8507, Japan
[e] Institute of Low Temperature Science, Hokkaido University, Sapporo, 060-0819, Japan
[f] Stevens Institute of Technology, Hoboken, 07030, USA

ARTICLE INFO

Article history:
Received 31 March 2021
Revised 15 June 2021
Accepted 19 July 2021
Available online 21 July 2021

Keywords:
Light scattering
Polarization
Neutral point
Reflectance
Snow
Bare ice

ABSTRACT

The properties of light reflected from snow and ice surfaces are important for the understanding of light scattering theory and the interpretation of remote sensing in the cryosphere. Spectral measurements of the degree of linear polarization (DoLP) and its related Stokes parameters $P_q = -Q/I$ and $P_u = U/I$ of Stokes vector $\mathbf{I}_S = [I\ Q\ U\ V]^T$ were made for various snow and ice surfaces in Hokkaido, Japan. The measurement results indicated that the angular dependence on both the viewing angle and azimuth angle in the DoLP, P_q and P_u was significant especially in the shortwave infrared (SWIR) regions. In addition, an important finding here is that the measurements revealed for the first time the existence of neutral points of P_q and P_u in the snow and bare ice surface. The SWIR polarization features can be explained by the single scattering properties of snow/ice or surface reflection associated with surface scattering. For the snow cases, the DoLP was represented by the measurement geometry and the scattering phase matrix while for the bare ice case, the DoLP was represented by the measurement geometry and the Fresnel reflection matrix. An additional remark is that the angular dependence of the neutral points was linked exclusively to the measurement geometry regardless of snow particle size, shape and scattering/absorbing inclusions in the ice. In contrast, the polarization in the visible regions was so small but remained detectable. However, the angular dependence of the neutral points was somewhat different from that in near infrared and SWIR regions. These results suggested that the neutral points depend on the polarization magnitude and the plane of polarization that related to the multiple scattering in the snow and atmosphere. The polarimetric measurements related to the neutral points are expected to be useful for the retrieval of new snow/ice physical parameters.

1. Introduction

The cryosphere is the most vulnerable area to the climate changes. The decreases in snow cover duration and area in the Northern hemisphere [1–3], and the retreat of glaciers in the Arctic area and ice sheet in Greenland [4,5] are typical phenomena. Snow highly reflects solar radiation and has the effect of controlling global warming. However, when snow cover decreases over time and space as a result of temperature rise, albedo decreases, resulting in further acceleration in the global warming through snow-albedo feedback [6,7]. For this reason, the cryosphere is an important observation target from the perspective of climate change monitoring.

Satellite observations are indispensable for the wide area snow-cover monitoring. Optical remote sensing has expanded from the use of panchromatic and multispectral sensors to imaging spectrometers with multi-viewing capability. Operational satellites such as Advanced Very High Resolution Radiometer (AVHRR), Moderate Resolution Imaging Spectroradiometer (MODIS), Second-generated Global Imager (SGLI), and Sentinel-series are capable of

* Corresponding author.
E-mail address: tanikawa@mri-jma.go.jp (T. Tanikawa).

https://doi.org/10.1016/j.jqsrt.2021.107845

high-resolution observation on spatial and temporal scales which give the opportunity to investigate large-scale changes of the cryosphere in response to climate changes. For example, snow coverage was monitored by satellite data acquired from the 1980s to the present and changes in snow coverage was analyzed [1,8,9]. In addition, retrievals of snow parameters such as snow grain size, mass concentration of light absorbing particles in snow, which are the primary parameters controlling spectral and broadband albedo, and snow/ice surface temperature were attempted [10–12]. These snow parameters were retrieved by Global Imager (GLI) in the Northern Hemisphere [13–15]. Afterwards, the snow grain size in the Antarctic and Greenland ice sheets has been monitored by many researchers and its spatial and temporal variations have been revealed [16–21]. These results are based on a large number of observational and simulation studies on spectral albedo and reflectance of snow related to the intensity of reflected light [22–30].

Light reflected from the surface can also be described in terms of its polarization properties [31–33]. Polarimetric observations have recently attracted much attention and their use is accelerating especially in the atmospheric and oceanic communities. The space-borne POLarization and Directionality of the Earth's Reflectances (POLDER) instrument, which was launched in 1996 on the Advanced Earth Observing Satellite (ADEOS) platform, provided the first quantitative measurements of the reflectance and polarization characteristics in atmosphere, land and ocean surface [34]. The POLDER instrument measured polarization that was used for cloud and aerosol microphysics retrievals [35,36]. NASA/GISS airborne Research Scanning Polarimeter (RSP) based on polarimetric and multi-angular measurements, provided accurate polarimetric measurements from land and ocean surfaces and retrieved various geophysical parameters [37,38].

On the other hand, for the land surface use, despite more than 30 years of experiments, practical applications have remained few. Though very few studies and limited information have been reported on the polarization properties of the snow surface, useful knowledge about the polarization is now emerging and being established. Goloub et al. [39] confirmed that a few percent of snow polarization were observed in the forward direction of POLDER data. Leroux et al. [40] examined the effect of snow grain shape on snow total and polarized reflectance from the comparison between the measurements and radiative transfer calculations, and found reflectance properties to be sensitive to snow grain size and shape. Though they only paid attention to the near-infrared spectral range at wavelength $\lambda = 1650$ nm, polarization has a potential to discriminate between clouds and snow surfaces. Perovich [41] measured polarized reflectance for various snow and sea ice surfaces at different polar and azimuth angles and confirmed the strong polarization from sea ice surfaces in the forward direction. Since the solar zenith angle was close to the Brewster angle, any specularly reflected light would be highly polarized. Tanikawa et al. [42] also confirmed the strong forward peaks for the melt-freeze crust in the near-infrared regions under the Brewster geometry. They concluded from measurement results that the polarization is quite sensitive to not only optical properties of snow but also the solar incident angle and illumination condition. The effect of a densely packed medium in snow polarization was theoretically studied based on ray-tracing simulations [43], and it was later confirmed by Lv and Sun [44] that the changes of the negative degree of linear polarization in the backward direction, which is a most remarkable observation phenomenon, were related to the packing density of snow. The polarization properties on snow grain size were extensively studied in the snow field and the cold laboratory [42,45,46]. These results suggested the polarization measurement will be helpful for the retrievals of snow grain size. Recently, radiative transfer models for the atmosphere-snow system were developed for the calculation of polarized radiance and reflectance, and their application to remote sensing were attempted [38,47].

There has been an extensive effort to investigate the area of the polarization of snow described above. The majority of research into the polarimetric properties of snow is concerned with the degree of linear polarization (DoLP). However, each element of Stokes vector (described in the next section) that makes up the DoLP has not been fully explored yet, so there is a possibility that different polarization information is acquired even with the same DoLP. Furthermore, as mentioned above, the DoLP depends on the snow grain size. But it is not completely understood how each element of Stokes vector relates to the snow grain size and the measurement geometries. The elements of Stokes vector are related to the magnitude and orientation of the semi-major axis of the polarization ellipse, which is expected to contain additional information concerning snow properties. More detailed investigations and analyses are thus required to understand and quantify certain polarization properties of snow.

We measured spectral DoLP and its related polarization parameters of snow and bare ice through intensive observations in Hokkaido, Japan. In this paper, we focus on the angular dependence of each element of the Stokes vector related to the magnitude and the orientation of the polarization for snow and bare ice surfaces, and discuss the utility of these parameters for characterization of the snow and the bare ice. In Section 2, definitions of terms and explanations of spectral measurements are presented. Section 3 covers measurement conditions about location, snow and atmospheric conditions. In Section 4, spectral DoLP and related parameters for various snow types and bare ice surfaces are reported. We discuss the angular dependence on the DoLP and its related parameters. Section 5 presents conclusions and future work.

2. Definition of radiant quantities and spectral measurements

2.1. Definition

The polarization state of light can be described by a set of four parameters specified by the symbols $I_{\parallel}$, $I_{\perp}$, U and V, which are elements of the Stokes vector $\mathbf{I}(\lambda) = [I_{\parallel}(\lambda)\, I_{\perp}(\lambda)\, U(\lambda)\, V(\lambda)]^T$. The Stokes parameters $I_{\parallel}(\lambda)$ and $I_{\perp}(\lambda)$ are the intensity components that are parallel and perpendicular to the scattering plane, respectively. $U(\lambda)$ is the degree of linear polarization in 45° and 135° planes to the reference plane, and $V(\lambda)$ is the degree of circular polarization which is usually negligible after reflection, and the superscript T denotes the transpose [32,48,49]. This Stokes vector is related to the more common one, $\mathbf{I}_S(\lambda) = [I(\lambda)\, Q(\lambda)\, U(\lambda)\, V(\lambda)]^T$, by $I(\lambda) = I_{\parallel}(\lambda) + I_{\perp}(\lambda)$ and $Q = I_{\parallel}(\lambda) - I_{\perp}(\lambda)$, where $I(\lambda)$ is the total intensity of the reflected light. The Stokes vector's first three elements are the most important ones determining the polarization state. The degree of linear polarization (DoLP) is described by

$$\mathrm{DoLP}(\lambda) = \sqrt{P_q^2(\lambda) + P_u^2(\lambda)}, \tag{1}$$

where $P_q(\lambda)$ and $P_u(\lambda)$ are polarization-related parameters normalized by $I(\lambda)$ as follows:

$$P_q(\lambda) = -\frac{Q(\lambda)}{I(\lambda)}, \quad P_u(\lambda) = \frac{U(\lambda)}{I(\lambda)}. \tag{2}$$

These above quantities also depend on the solar-target-sensor geometry, i.e. on the solar zenith and azimuth angles (θ_0, ϕ_0) and the sensor's viewing and azimuth angles (θ_v, ϕ_v) respectively, so DoLP, P_q and P_u depend on θ_0, θ_v, ϕ_0 and ϕ_v.

In this paper, we provide the hemispherical-directional reflectance factor (HDRF) in order to examine the relation between

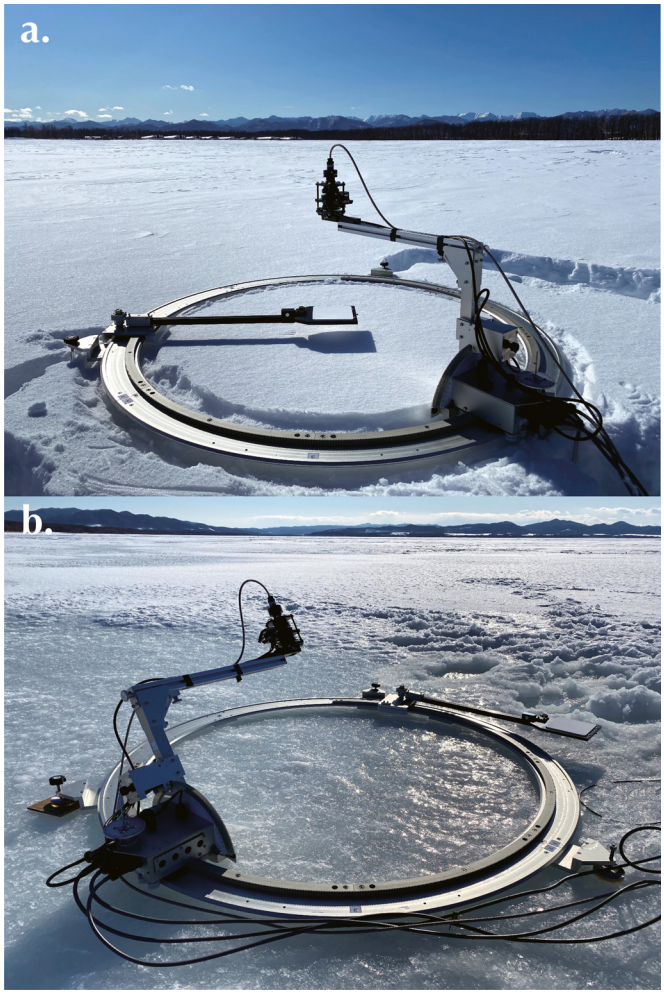

Fig. 1. Photographs of the goniometer to measure the polarized radiation: (a) The downward solar flux was measured by directing the optical fiber through the fore optics with polarizer to the upper surface of the WRS, and (b) The upward polarized radiance was directly measured by the optical fiber through the fore optics with polarizer. Photographs were taken at the snow surface at Nakasatsunai (a) and at the bare ice surface at Saroma-ko Lagoon (b).

DoLP and HDRF. The HDRF is defined by

$$\mathrm{HDRF}(\theta_0, \theta_v, \phi_0, \phi_v; \lambda) = \frac{\pi I(\theta_0, \theta_v, \phi_0, \phi_v; \lambda)}{F(\theta_0; \lambda)}, \quad (3)$$

where I is the upward radiance reflected from the surface and F is the downward solar irradiance for the surface which includes radiation from the entire hemisphere.

2.2. Spectral polarization measurements

The spectral measurements were made using grating spectrometers, ASD FieldSpec 4 (Malvern Panalytical, UK). The scanning spectral range of the instrument is from the ultraviolet to the near infrared wavelength region between $\lambda = 350$ nm and 2500 nm with a spectral resolution of 3 nm for $\lambda = 350 - 1000$ nm and 10 nm for $\lambda = 1001 - 2500$ nm, and a spectral sampling (bandwidth) of 1.4 nm for $\lambda = 350 - 1000$ nm and 1.1 nm for $\lambda = 1001 - 2500$ nm. The scanning time employed was 0.1 s with a sampling interval of 1 nm for the full spectral range. Angular dependence of DoLP and its related parameters was observed by a self-developed goniometer (Fig. 1). This instrument was upgraded from a previous version used in the studies reported by Tanikawa et al. [42] and observes the same point of the target from any polar and azimuth angle. The polar and azimuth angles can be set with an accuracy better than 1° by a machine control device.

The polarized radiance reflected from the snow and bare ice surfaces was brought into the spectrometer by a calcite Glan-Thomson prism installed in the fore optics. By machine control devices, the calcite Glan-Thomson prism was rotated in an increment of 1° to measure the polarized radiation of different directions. A quartz-wedge depolarizer was inserted between the optical fiber and polarizer in order to prevent a linearly polarized radiation entering the spectrometer. The field of view of this system is 7°. The Stokes vector's first three elements are derived by measuring the reflected polarized radiance at different polarizer directions as follows:

$$I(\lambda) = \{L_{0^\circ}(\lambda) + L_{45^\circ}(\lambda) + L_{90^\circ}(\lambda) + L_{135^\circ}(\lambda)\}/2, \quad (4)$$

$$Q(\lambda) = L_{0^\circ}(\lambda) - L_{90^\circ}(\lambda), \quad (5)$$

$$U(\lambda) = L_{45^\circ}(\lambda) - L_{135^\circ}(\lambda), \quad (6)$$

where $L_x(\lambda)$ is the polarized radiance at different polarizer directions x ($x = 0^\circ, 45^\circ, 90^\circ$ and 135°). For the HDRF measurement, the downward solar irradiance was observed by directing of optical fiber through the foreoptics with polarizer to the upper surface of the white reference standard (WRS) placed on the plate (Fig. 1a).

The measurement was made for various planes including the principal and the perpendicular plane with the viewing angle θ_v of basically every 10° from 0° (nadir) to 70°. During the measurement, the fore optics holds pointing to the same target of the snow/bare ice surface from any polar and azimuth angle, but the footprint of the measured surface varies with the polar angle. The configuration of this upgraded goniometer is the same as the previous one [42]. So, the distance from the target point to sensor was 50 cm. The footprint was a circle with a diameter of 6.1 cm at $\theta_v = 0^\circ$ and an ellipse with a major axis of 12.3 cm at $\theta_v = 60^\circ$.

The average measurement uncertainty of this system was estimated within 3% based on the error analysis process represented by Suomalainen et al. [50]. Comparing to the previous version [42], the measurement uncertainty was reduced due to mainly the power angle adjustments of the goniometer and the polarizer direction, and the wedge depolarizer installed in the measurement system.

3. Observation conditions

3.1. Observation site

The spectral measurements were carried out for snow fields on February 11–14, 2020 at Nakasatsunai, Hokkaido, Japan (located at 42°38'40"N, 143°06'36"E), and for smooth bare ice fields on February 25, 2020 at Saroma-ko Lagoon, Hokkaido, Japan (located at 44°07'21"N, 143°57'59"E). The observation site at Nakasatsunai is located at the east side of Hokkaido close to the Pacific Ocean. The measurement was conducted at snow-covered flat farms without any undulation and shadows by forest. The site at Saroma-ko Lagoon (surface area, 151.59 km^2 and maximum depth, 22 m) is located on the northeast coast of Hokkaido and is connected to the southern part of the Sea of Okhotsk through two inlets. The measurement was conducted at smooth bare ice area of the lagoon where there is no obstacle of ridge and so on.

3.2. Snow/bare ice condition

Snow pit work was conducted together with spectral measurements in order to explain various spectral data quantitatively. The

snow physical parameters measured here were as follows: snow depth, snow form (shape), snow grain size, snow temperature, snow density and mass concentration of light absorbing particles in snow. The snow grain shapes are according to "The International Classification for Seasonal Snow on the Ground" [51]. The grain size was defined as half the branch width of dendrites, as half of the width of the narrower portion of broken crystals, or the radius of each spherical particle. This dimension corresponds to r_2 defined by Aoki et al. [25]. Because its use in radiative transfer calculations led to good correlations between spectral albedo and r_2 [25,52] and between broadband albedo and r_2 [53], the dimension of r_2 is considered to be the optically equivalent snow grain size [51]. Hence, the dimension of r_2 was employed as snow grain size in this study.

Snow samples were collected to estimate the mass concentration of light absorbing particles in snow (insoluble solid particles in the snowpack; hereafter snow impurities). The concentration of snow impurities is an essential parameter controlling snow albedo in the visible regions [23]. We measured it from two snow layers of d_s=0–2 cm depth and d_s = 2–10 cm depth where d_s is snow depth. The mass concentration of dust, elemental carbon (EC) and organic carbon (OC) were determined in our laboratory by filtering melted snow samples and by the instrument of the Lab OC-EC Aerosol Analyzer (Sunset Laboratory Inc., Tigard, Oregon) based on the thermal optical reflectance method [54]. We followed the same approach by Kuchiki et al. [55] in the instruments and measurement procedures. So we omitted the explanation in details.

Fig. 2 shows the results of the vertical profiles of snow physical parameters. For Nakasatsunai site (Fig. 2a-b) the observed snow form in top layer consists of mainly decomposing and fragmented precipitation particles and faceted crystals in February 11, and melt forms (melt-freeze crust) in February 14. Snow grain size gradually increased day by day during the intensive field campaign. The snow impurity concentration was on the order of ppmw and results of OC, EC and dust indicated almost the same value during the measurements. For Saroma-ko lagoon site (Fig. 2c), the surface layer was smooth bare ice and specular reflection was confirmed (Fig. 1b). This is a refreezing ice of melted-snow partly including seawater. The layer below the surface consisted of melt forms with slush.

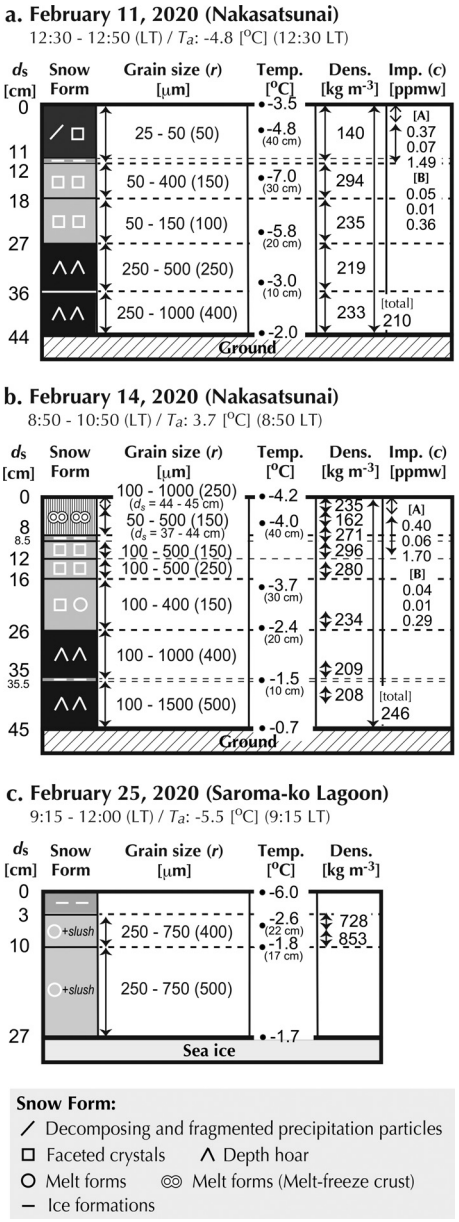

Fig. 2. Vertical profiles of snow physical parameters: (a) February 11, 2020, (b) February 14, 2020 at Nakasatsunai and (c) February 25, at Saroma-ko lagoon. For snow grain size (r), minimum, maximum and medium (within brackets) values are described. Mass concentration of snow impurities has three values, OC, EC, and dust, respectively. It was measured for two snow layers of [A] d_s=0–2 cm depth and [B] d_s = 2–10 cm depth. The meaning of an abbreviation is as follows: local time (LT), air temperature (T_a), snow depth (d_s), snow temperature (Temp.), snow density (Dens.) and mass concentration of snow impurities (Imp.).

3.3. Atmospheric condition

In order to evaluate the state of polarization of snow and bare ice surfaces, measurements under clear sky conditions are required. We monitored the cloud amount and the aerosol optical thickness (AOT). The cloud condition was monitored by visual observations and all sky camera. The spectrometer was also used to measure the solar illumination condition. The diffuse fraction of the downward solar flux is a reliable guide for the presence of clouds. The AOT at $\lambda = 380, 440, 675$ and 870 nm was measured by a Sunphotometer (Microtops-II, Solar Light Inc., Glenside, Pennsylvania). However, we were unable to measure the AOT at Saroma-ko lagoon site due to a lack of the equipment.

Fig. 3 shows the AOT and the diffuse fraction during the spectral measurements. Cloud amounts were almost zero by the visual observations and all sky camera. Although the AOT and the diffuse fraction gradually increased day by day at Nakasatsunai site (on February 11, 12 and 14), the results of the diffuse fraction can be considered as a clear sky Rayleigh atmosphere. Since cloud cover increases the diffuse solar fraction for all spectral regions, we would say from Fig. 3 that spectral measurements were conducted under clear sky conditions.

4. Results and discussion

4.1. Spectral dependence on the DoLP, P_q, P_u and HDRF

Fig. 4 depicts spectral DoLP and its related polarized parameters P_q and P_u at $\lambda = 350 - 2500$ nm for the precipitation particles taken at Nakasatsunai site on February 11, 2020. Spectral data at several viewing angles in the forward direction ($\Delta\phi = 0°$), sideward direction ($\Delta\phi = 90°$) and backward direction ($\Delta\phi = 180°$) were depicted. In this paper, we refer to the directions of $0 \leq \Delta\phi \leq 60°$, $60° < \Delta\phi \leq 120°$ and $120° < \Delta\phi \leq 180°$ as the "forward direction", "sideward direction", and "backward direction", respectively. The solar zenith angles were $\theta_0 = 57°$ corresponding

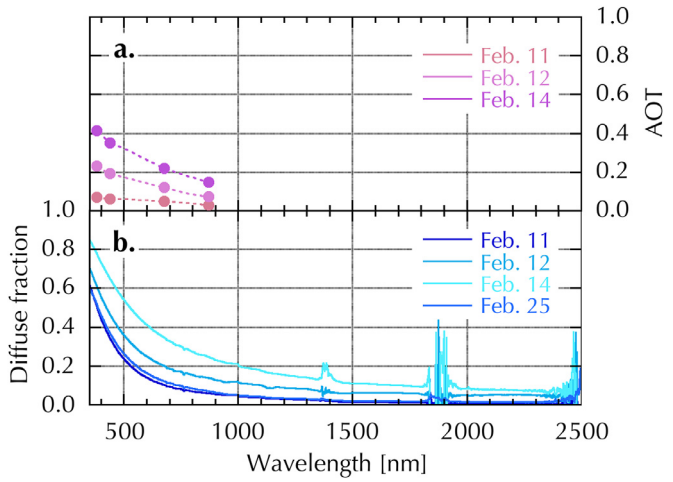

Fig. 3. (a) Aerosol optical thickness (AOT) and (b) diffuse fraction of the downward solar flux. All data were measured during the intensive field measurements. For (b), the spectral data between $\lambda = 1800$ and 2000 nm and $\lambda > 2400$ nm are noisy because signal-to-noise ratios were low in the absorption bands by atmospheric gases. Note that we also showed the data on February 12, 2020 though we didn't discuss spectral data of this day in this research, and there are no AOT data available on (a) February 25, 2020 at Saroma-ko lagoon site.

to local solar noon. The spectral data at $\lambda = 1800 - 2100$ nm and $\lambda > 2300$ nm were masked due to low signal-to-noise ratios in absorption bands of atmospheric gases. For a reference, results of spectral HDRF data were depicted.

The spectral DoLPs in the visible region (VIS; $\lambda = 400 - 700$ nm) were small in the range between 0.0 and 0.03 and spectrally uniform. There was no clear dependence on the relative azimuth angle. Because the light absorption by the ice is particularly weak in VIS regions [56], multiple scattering is dominant, implying that the light reflected from the snow surface was essentially unpolarized. In the near infrared (NIR; $\lambda = 700 - 1400$ nm) and the shortwave infrared (SWIR; $\lambda = 1400 - 2500$ nm) regions, wavelength dependence of the DoLP with unique spectral features was confirmed. Some sharp peaks at $\lambda = 1500$ and ~ 2100 nm and some troughs between each peak corresponded to the light absorption by ice. This result can be explained by the difference of the contribution of volume scattering to the reflected light as follows [42]. The volume scattering originates from the spectral dependence of the absorption coefficient by ice. So, for highly absorbing spectral regions, the volume scattering is relatively low. In other words, scattering process at a surface is dominant for the reflected light. Hence, the reflected light is polarized for highly absorbing spectral regions, which explains the characteristic measured spectral features in the NIR and SWIR regions. These features are consistent with the results of previous studies conducted in the cold laboratory and field measurements [42,44–46].

The dependence of the DoLP on the viewing angle was mainly observed in the SWIR regions. This result can be seen in the previous studies [42,44–46], but it is interesting to note that the viewing angle dependence was different between the DoLP and the HDRF; the viewing angle corresponding to the maximum values were different from each other. Similar results for other cases were obtained. This result will be discussed in the next section.

Regarding the linear polarization parameters P_q and P_u, the DoLP in the principal plane ($\Delta\phi = 0^\circ$ and 180°) is determined by $P_q > 0$ and $P_u \sim 0$, respectively (Fig. 4a and c). In general, the U Stokes parameter would be 0 in the principal plane, so that Q is dominant in the DoLP. In contrast, the DoLP in the perpendicular plane (sideward direction; $\Delta\phi = 90^\circ$) depends on both $P_q < 0$ and $P_u < 0$ (Fig. 4b). So, the DoLP is the result of combining the polarizations of both Q and U. Furthermore, we found that the weak

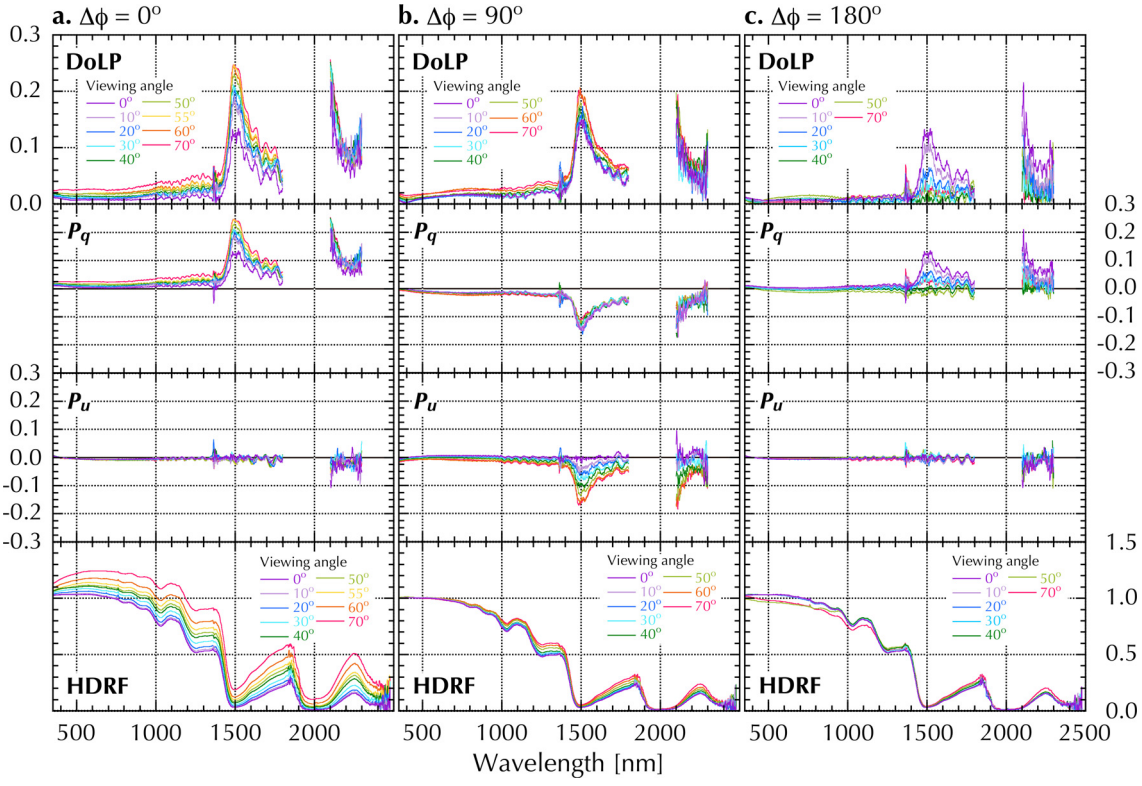

Fig. 4. Spectral DoLP, P_q, P_u and HDRF at several viewing angles in the forward direction ($\Delta\phi = 0^\circ$), sideward direction ($\Delta\phi = 90^\circ$) and backward direction ($\Delta\phi = 180^\circ$), respectively, taken at February 11, 2020. $\theta_0 = 57^\circ$. Note that DoLP, P_q, P_u between $\lambda = 1800$ nm and 2100 nm and for $\lambda > 2300$ nm were masked due to the low signal to noise ratios in the atmospheric gaseous absorption bands. Spectral data for $\theta_v = 60^\circ$ in the backward direction ($\Delta\phi = 180^\circ$) were masked due to the detector shadow.

dependence of the DoLP on viewing angle was mainly due to P_u, since P_q would be independent of the viewing angle. In summary, the behavior in Q and U was different even in the same DoLP, depending on the azimuth angle, and besides that, the viewing angle dependence in Q and U was different in the azimuth angle. In the next section, we will further examine the effect of the viewing and azimuth angles on the DoLP and related parameters P_q and P_u.

4.2. Angular dependence on the DoLP and related parameters P_q and P_u

Figs. 5–7 show polar contour plots of measured HDRF, DoLP, P_q and P_u for the snow and bare ice surfaces in SGLI selected channels at $\lambda = 443, 673.5, 868.5$ and 1630 nm. These wavelengths are used in the snow parameter retrievals adopted for the SGLI snow/ice products [21], and actually SGLI has two polarization channels at $\lambda = 673.5$ and 868.5 nm that can measure polarization [57]. These four wavelengths selected here were similar to the spectral channels of satellite instruments such as MODIS and POLDER as well as RSP. Thus, HDRF, DoLP, P_q and P_u shown in Figs. 5–7 were computed using the spectral response functions of SGLI [57]. All measurements were conducted under clear sky condition for $\theta_0 = 52^\circ \sim 62^\circ$. For the bare ice measurements, θ_0 was almost equal to the Brewster angle ($\theta_B \sim 52^\circ$).

4.2.1. DoLP

At first, we discuss the DoLP of snow surface. Fig. 5 shows results for the precipitation particles at February 11, 2020, while Fig. 6 depicts results for the melt forms at February 14, 2020. The DoLP plots were characterized by high values in the forward direction ($\Delta\phi = 0^\circ$) that gradually decreased toward the side and backward directions even at $\lambda = 443, 673.5$ and 868.5 nm. The angular dependence of the DoLP on the viewing geometry at these three wavelengths was commonly very small and the DoLP in the forward direction was less than 0.03. Because multiple scattering is dominant due to relatively weak light-absorption by ice at these wavelengths [56], the radiances were almost unpolarized.

In contrast, the dependence of the DoLP on viewing angle was clearly seen at $\lambda = 1630$ nm. The DoLP appears to exhibit a broad peak in the forward and sideward directions of $\Delta\phi < 90^\circ$. This polarization feature can be seen in both cases (Figs. 5 and 6); as a general trend, the DoLPs of the melt forms were higher than those of the precipitation particles. These results can be explained in terms of single scattering properties of snow particles using a simple scattering theory. In the SWIR regions where the light absorption by ice is relatively strong, the scattering process will be dominated by the single scattering at the surface layer. So, for unpolarized incident solar radiation $\mathbf{I}_0 = [I_0\ 0\ 0\ 0]^T$ where I_0 is the unpolarized intensity, the scattered radiation after one scattering event $\mathbf{I}_1 = [I_1\ Q_1\ U_1\ V_1]^T$ can be described as follows:

$$\mathbf{I}_1(\Theta, \sigma_1, \sigma_2) = \mathbf{L}(-\sigma_2)\mathbf{F}(\Theta)\mathbf{L}(\pi - \sigma_1)\mathbf{I}_0 \tag{7}$$

$$= \begin{bmatrix} a_1(\Theta)I_0 \\ \cos 2\sigma_2 b_1(\Theta)I_0 \\ -\sin 2\sigma_2 b_1(\Theta)I_0 \\ 0 \end{bmatrix}, \tag{8}$$

where $\mathbf{F}(\Theta)$ is the normalized scattering matrix, $\mathbf{L}$ is the rotation matrix, and Θ is the scattering angle. a_1 and b_1 are elements of normalized scattering matrix $\mathbf{F}$, and σ_1 and σ_2 are the angles of rotation (see Appendix A). The normalized scattering matrix $\mathbf{F}$ generated by electromagnetic scattering theory provides a complete characterization of the angular distribution and polarization state of the light scattered by an ensemble of dielectric particles [58].

These values are connected with measurement geometries of θ_0, θ_v, and $\Delta\phi (= \phi_v - \phi_0)$ using spherical trigonometry [33]:

$$\cos\Theta = -\cos\theta_v \cos\theta_0 + \sin\theta_v \sin\theta_0 \cos\Delta\phi, \tag{9}$$

$$\cos\sigma_1 = \frac{\cos\theta_v + \cos\theta_0 \cos\Theta}{\sin\theta_0 \sin\Theta}, \tag{10}$$

$$\cos\sigma_2 = -\frac{\cos\theta_0 + \cos\theta_v \cos\Theta}{\sin\theta_v \sin\Theta}. \tag{11}$$

Thus, $\mathbf{I}_1$ can be represented using the measurement geometries, that is $\mathbf{I}_1(\theta_0, \theta_v, \Delta\phi)$. Details of the normalized scattering matrix $\mathbf{F}$ and its related coordinate system are described in Appendix A. From the Stokes parameters of $\mathbf{I}_1$, we obtain the DoLP as follows:

$$\text{DoLP} = \mid b_1(\Theta)/a_1(\Theta) \mid . \tag{12}$$

Fig. 8 shows the ratio $-b_1/a_1$ of elements of normalized scattering matrix for various snow grain sizes and shapes calculated by the geometrical optics approximation [59,60] and the Mie theory. In general, this ratio indicates the degree of the linear polarization of scattered light for unpolarized incident light in a single grain and is a function of a scattering angle Θ. From the results, the ratio reveals a broad peak at approximately $\Theta = 60^\circ - 120^\circ$ at $\lambda = 1630$ nm regardless of the shape and size of the particles. This means that the scattered light in this range of scattering angles would be polarized. Based on this result, we investigated the relationship between the broad peak of the DoLP and the scattering angle Θ calculated from θ_0, θ_v and $\Delta\phi$ by Eq. (9) and found that the broad peak of the DoLP corresponds to around $\Theta = 60^\circ - 120^\circ$ (Figs. 5d and 6d). It is concluded that the broad peak of the DoLP results from the polarimetric properties of the single scattering properties of snow particles. Regarding the difference between DoLP of the precipitation particles and that of the melt forms, it is considered from Fig. 8 that the dependence on the snow grain size would be reflected in the measured DoLP.

As can be seen in the previous section, the dependence on viewing angle was different between the DoLP and the HDRF; the viewing angle corresponding to the maximum values were different from each other, and the maximum values were at $\theta_v = 30^\circ - 60^\circ$ for the DoLP, but at $\theta_v = 70^\circ$ for the HDRF. Both features can be explained by the single scattering properties of snow particles. Since the reason for the DoLP has already described above, the reason for the HDRF can be described as follows: From the relationship between the particle size and the wavelength, the scattered light intensity is dominant in the forward direction (see in Fig. 3 in Tanikawa et al. [30]); the smaller the scattering angle, the higher the scattered intensity. Therefore, the HDRF has a relatively higher value in the forward direction with the larger viewing angle where the scattering angle is small. This is the reason why the angular distribution was different between the DoLP and the HDRF.

Next, we discuss the DoLP of the bare ice surface shown in Fig. 7. The DoLP had strong peaks around $\theta_v = 40^\circ - 60^\circ$ in the forward direction for all four wavelengths. The DoLP at $\lambda = 1630$ nm was almost 1.0. This result is caused by a large specular reflection component plus strong polarization near the Brewster angle. Under the measurement condition of $\theta_0 = 53^\circ - 54^\circ$, the viewing angle $\theta_v = 40^\circ - 60^\circ$ along the principal plane was approximately equal to the angle of reflection, where there is a large specular component in the reflected light. Also, near Brewster's angle the specularly reflected light is strongly horizontally polarized. Thus, the high DoLP was mainly a result of specular reflection at $\theta_0 \sim \theta_B$. At other angles away from Brewster's angle, where the specular reflection was smaller, there was much less linear polarization of the reflected light. The reason is that the reflected light mainly consists of the volume scattering component which is largely unpolarized. However, surface reflection is essentially independent

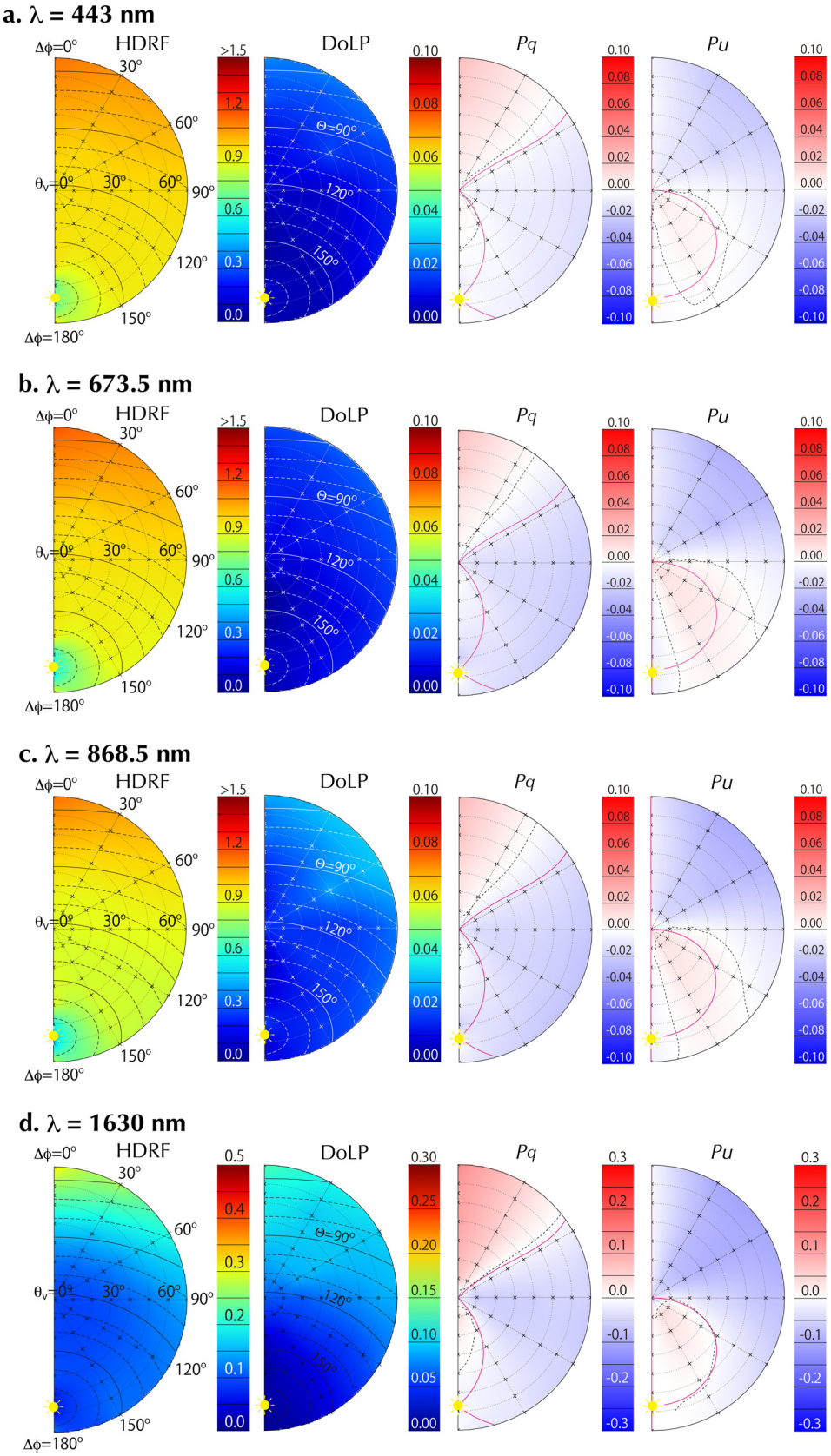

Fig. 5. Polar contour plots of HDRF, DoLP, P_q and P_u at four selected SGLI channels as obtained from spectral measurements for the precipitation particles on February 11, 2020. The small cross signs on each contour plot indicate observation points. The radial coordinate is proportional to the viewing angle θ_v. The centre of the half-circle is $\theta_v = 0^\circ$ (nadir) and the outer half-circle is $\theta_v = 70^\circ$. The illumination from the sun comes from the lower half of each map, indicated by the yellow sun mark. The solar zenith angle is $\theta_0 = 57^\circ$. The solid and dashed lines in the HDRF and DoLP plot the scattering angle Θ with 10° interval, while the black dash and red solid lines in the P_q and P_u indicate observed and calculated neutral points, respectively. The top of each contour map is the forward scattering direction. The values around the yellow sun mark in the HDRF are low because of the detector shadow. (For interpretation of the references to colour in this figure legend, the reader is referred to the web version of this article.)

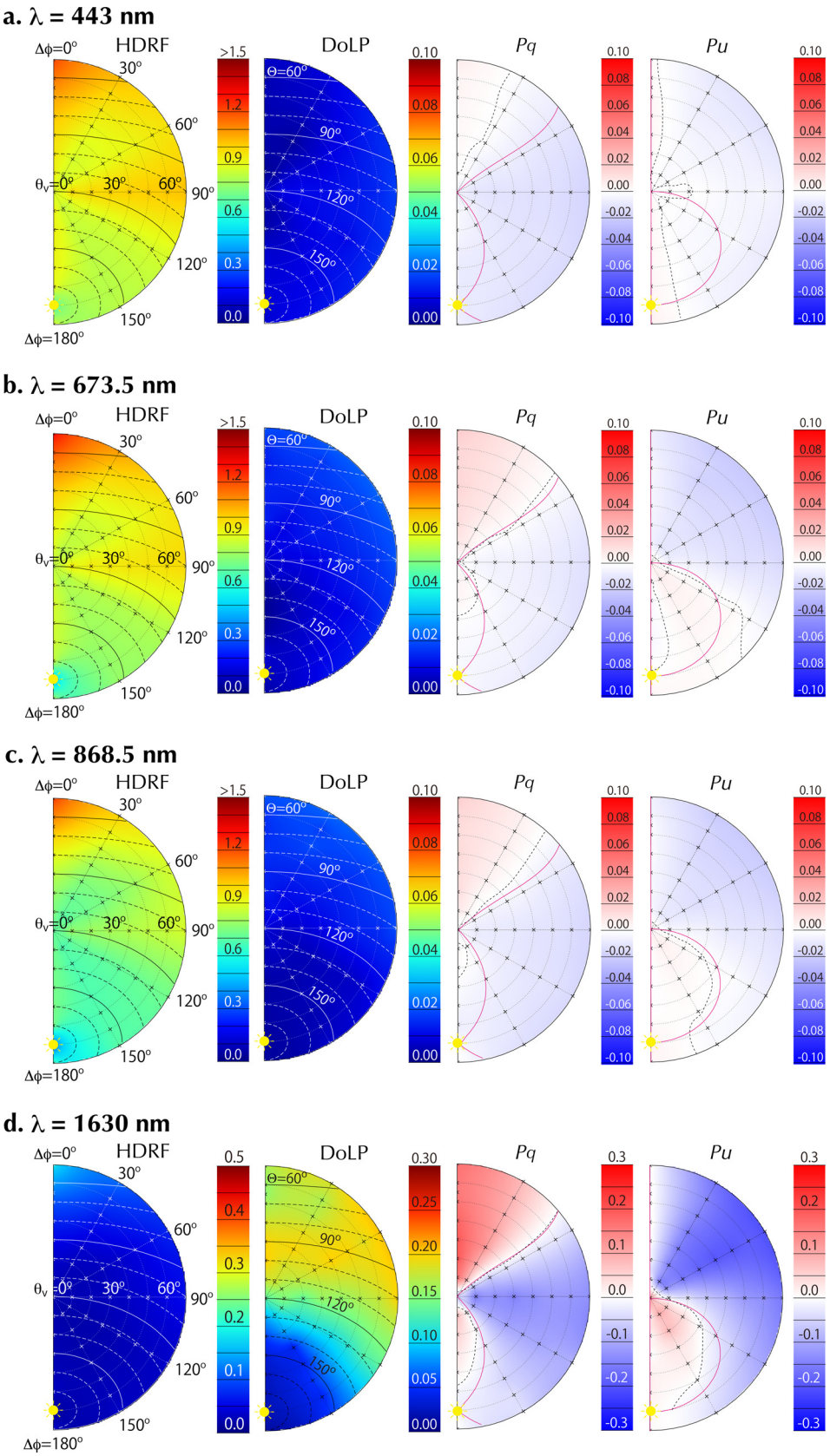

Fig. 6. Same as Fig. 5, but for the melt forms on February 14, 2020. $\theta_0 = 58^\circ - 61^\circ$.

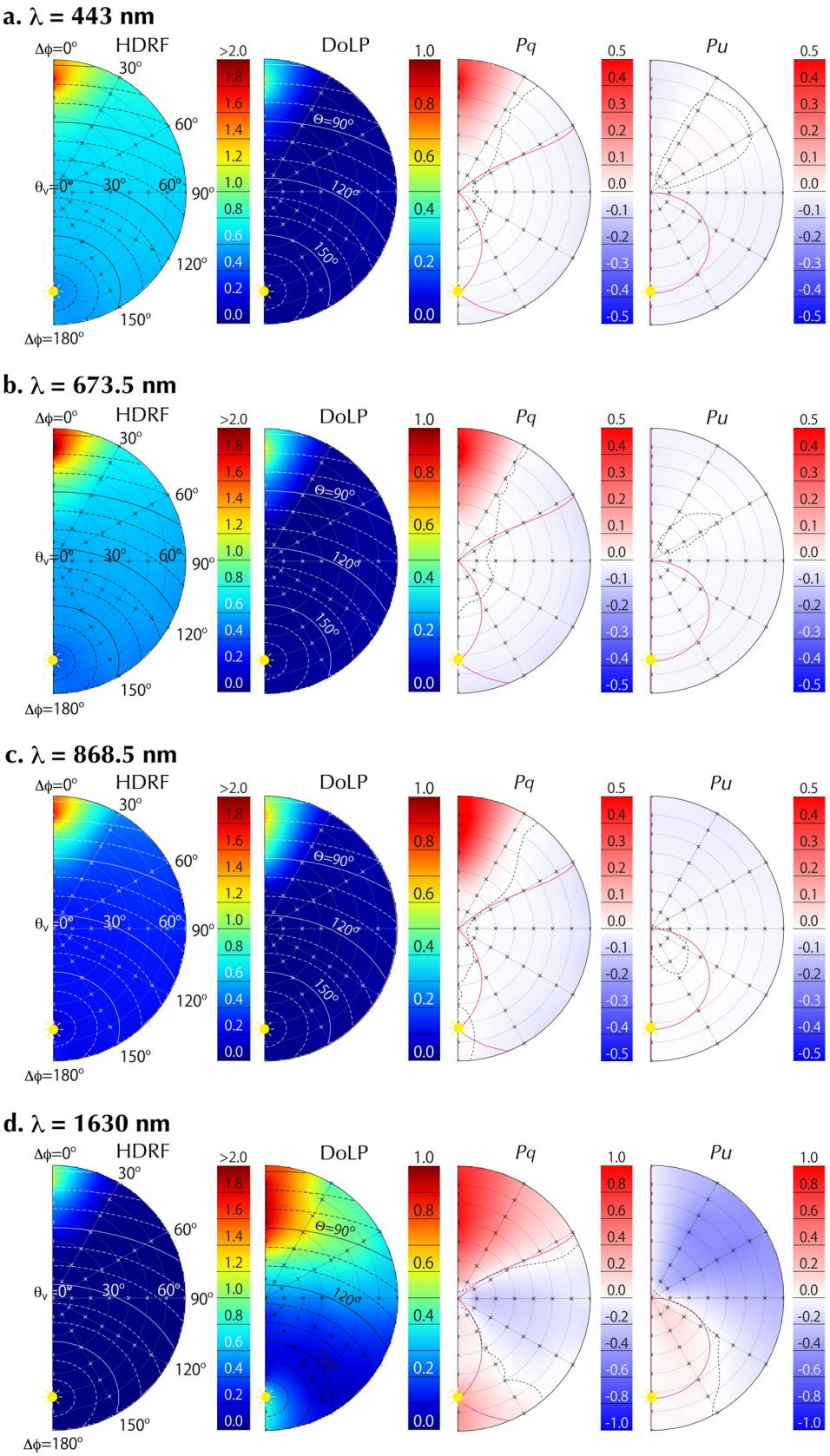

Fig. 7. Same as Fig. 5, but for the bare ice surface on February 25, 2020. $\theta_0 = 53^\circ - 54^\circ$.

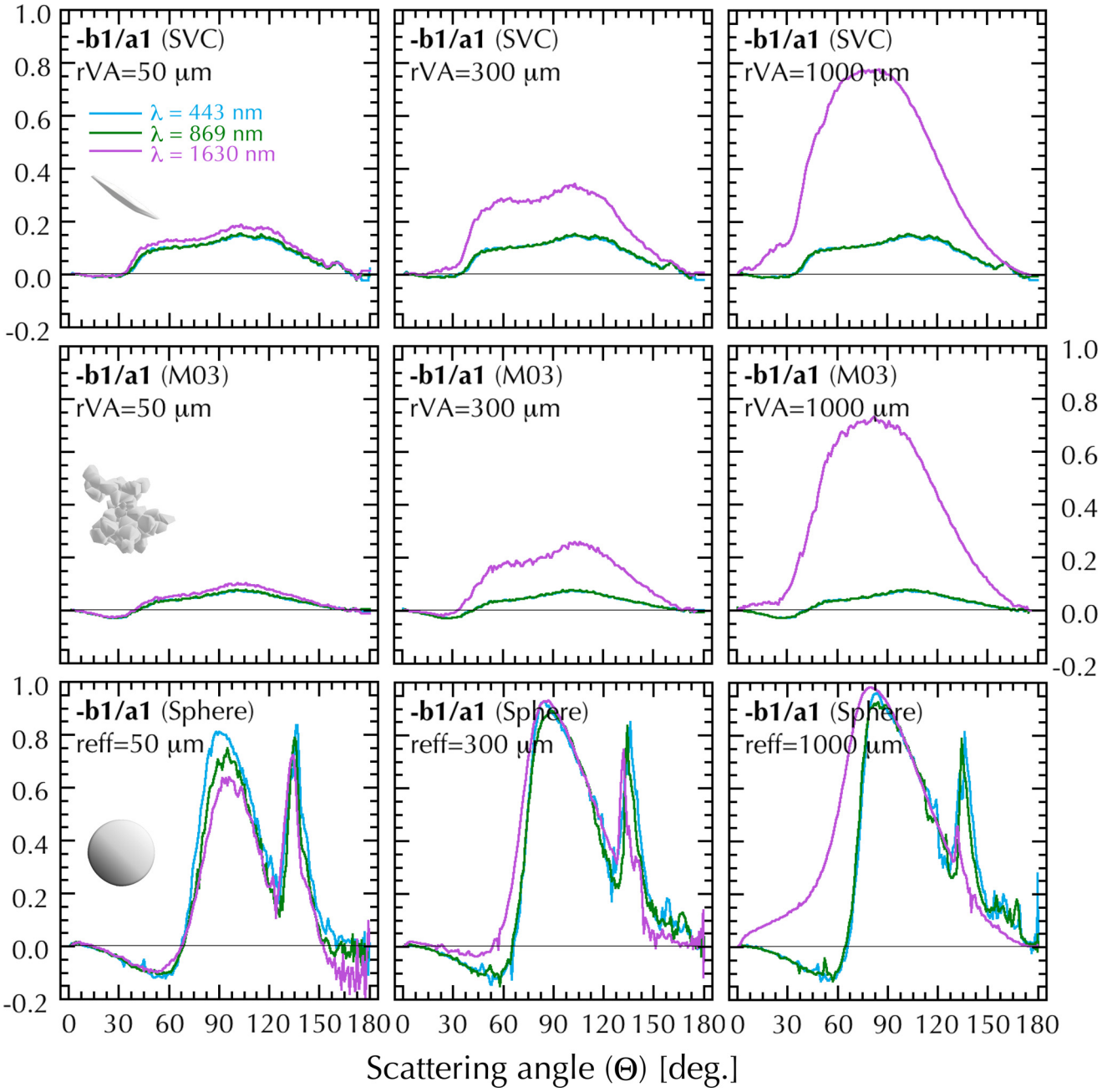

Fig. 8. The ratio $-b_1(\Theta)/a_1(\Theta)$ of the elements of normalized Stokes scattering matrix in the various snow grain size and shape: Voronoi column (SVC), Voronoi aggregate (M03) and spherical particles, respectively. *r*VA is the effective snow grain radius of Voronoi particles defined as radius of sphere that has an equal volume/area ratio [24], and r_{eff} is the effective radius of spherical particles. For the Voronoi particles, the ratios at $\lambda = 443$ nm and 869 nm are almost the same.

of wavelength, while the volume component is reduced at longer wavelength due to increased light absorption by the ice, implying that a noticeable polarization can be measured at $\lambda = 1630$ nm even at angles away from Brewster's angle. We note that the viewing angle corresponding to the maximum DoLP was different between the three wavelengths ($\lambda = 443, 673.5$ and 868.5 nm) and $\lambda = 1630$ nm. This might be due to the surface roughness in the bare ice surface (Fig. 1b). If the bare ice surface was to be perfectly smooth, one would expect to measure high DoLP values at almost the same viewing angle at $\lambda = 443, 673.5$ and 868.5 nm.

4.2.2. P_q and P_u

In this section, we focus on the angular dependence of P_q and P_u for light reflected from a snow surface (Figs. 5 and 6). By definition, both values were measured to be in the range below the DoLP. So, P_q and P_u were small values at $\lambda = 443, 673.5$ and 868.5 nm but they showed a remarkable dependence on the viewing geometry. P_q had positive values in the forward direction and then the sign was inverted from the side to the backward directions, and P_q exhibited zero and negative values except for some angles. In contrast, P_u was almost zero in the principal plane, had negative values in the forward direction except for the principal plane, and had positive values in the backward direction. The neutral points ($P_q = 0$ and $P_u = 0$) were continuously observed. For P_q, neutral points were observed in the forward and backward directions, while for P_u, neutral points were observed in the backward direction. An even more interesting result is that the signs and neutral points of P_q and P_u are almost independent of viewing geometry especially for NIR and SWIR wavelengths, though they are not completely the same positions. This result can be seen in both

snow surface measurements of the precipitation particle and melt form: the snow conditions have little effect on the position of the signs and the neutral points. This circumstance would be indicative of a universal property of the polarization. These measurements represent the first known confirmation of these unique snow polarization features.

We now examine the position of the signs and the neutral points of P_q and P_u for the snow case. First, we consider the wavelength of $\lambda = 1630$ nm using a same approach as for the DoLP. If the single scattering in the surface layer is assumed to be dominant, then P_q and P_u can be represented from $\mathbf{I}_1$ (Eq. (8)) as follows:

$$P_q = -\cos 2\sigma_2 \cdot b_1(\Theta)/a_1(\Theta), \tag{13}$$

$$P_u = -\sin 2\sigma_2 \cdot b_1(\Theta)/a_1(\Theta), \tag{14}$$

where b_1/a_1 is again the ratio of elements of the normalized scattering matrix. Thus, the signs and the neutral points of each P_q and P_u would be determined by Eqs. (13) and (14). From this equation, the neutral points in P_q ($P_q = 0$) can be seen to require a measurement angle corresponding to the following condition: (i) principal plane ($\phi_v - \phi_0 = 0$): $\sigma_2 = 0$ or π (see Fig. A.9), so $\cos 2\sigma_2 = 1$, implying that the measurement angle must satisfy $-b_1(\Theta)/a_1(\Theta) = 0$, and (ii) the others ($\phi_v - \phi_0 \neq 0$): $\cos 2\sigma_2 = 0$ regardless of $-b_1(\Theta)/a_1(\Theta)$. An important point here is that the neutral point is independent to the snow grain size and shape. For $P_u = 0$, the following condition is required: (i) principal plane ($\phi_v - \phi_0 = 0$): $\sigma_2 = 0$ or π, so $\sin 2\sigma_2 = 0$, implying that P_u would be everywhere zero in the principal plane, and (ii) the others ($\phi_v - \phi_0 \neq 0$): $\sin 2\sigma_2 = 0$ regardless of $-b_1(\Theta)/a_1(\Theta)$. The neutral point in P_u is also independent of the snow grain size and shape.

Figs. 5d and 6d show polar contour plots of P_q and P_u and calculated neutral points at $\lambda = 1630$ nm. Each neutral point is seen to be consistent with the measured one. Also, each sign of P_q and P_u was consistent with the measured one, respectively, under the following condition: $P_q(P_u) > 0$ for positive sign and $P_q(P_u) < 0$ for negative sign in Eqs. (13) and (14). It is concluded that in the SWIR regions where the single scattering at the surface is dominant, the signs of P_q and P_u and the neutral points can be determined from the measurement geometric conditions irrespective of the snow grain size and the shape.

On the other hand, the angular dependence of P_q and P_u in the VIS and NIR regions was weak, but not cancelled completely. A weak dependence on the viewing geometry was still confirmed. This reason could be that the contribution to the reflected radiation of the surface scattering is higher than that of the volume scattering. But, the signs and neutral points of P_q and P_u did not completely match in all four wavelengths. For example, there exists a slight difference of the neutral points among them. Comparing to the neutral points at $\lambda = 1630$ nm, the neutral points for P_q at other three wavelengths seemed to be shifted forward, while the neutral points for P_u seemed to be broad in the backward direction. This difference may be related to the scattering properties in each wavelength. Because scattering by larger particles such as snow is characterized by strong forward scattering with a diffraction in the forward direction, and because the multiple (volume) scattering component is increased at shorter wavelength such as VIS, the scattered light penetrates in the forward direction, resulting in the difference among all four wavelengths. This could be the reason why the calculated neutral points based on the single scattering were not consistent with the measured ones in the VIS and NIR regions. According to radiative transfer calculations in the atmosphere-ocean system, the position of the neutral points indicated the difference in atmospheric conditions due to multiple scattering [61]. Thus, we conjecture that the snow layer structure and the atmospheric condition are related to the position of the signs and the neutral points.

We next focus P_q and P_u for the bare ice surface (Fig. 7). The angular dependence on the signs of P_q were mostly the same as for the snow case: P_q had positive values in the forward direction and then the sign was inverted from the side to the backward directions, and P_q exhibited zero and negative values except for some angles. But, the P_q in the forward direction was high in all four wavelengths comparing to the snow. In contrast, P_u was almost zero in the principal plane, and had positive values in the forward direction at $\lambda = 443$ nm and 673.5 nm and in the backward direction at $\lambda = 868.5$ nm and 1630 nm. The neutral points each were continuously observed. But, the positions of the neutral points of P_q and P_u were different between the bare ice and snow except for those at $\lambda = 1630$ nm.

We now examine the position of the signs and the neutral points at $\lambda = 1630$ nm based on the same approach as for the snow case. In the SWIR regions, the scattering process will also dominate reflection at the bare ice surface. However, the surface condition is different between the snow and the bare ice because the bare ice is not an aggregate of ice particles but a smooth surface. So, we applied a Fresnel reflection matrix $\mathbf{R}$ instead of the scattering matrix $\mathbf{F}$ in the scattering calculations. If $r_\parallel$ and $r_\perp$ are Fresnel reflection coefficients due to the change in refractive index n at the air-ice interface, P_q and P_u would be expected as follows:

$$P_q = -\cos 2\sigma_2 \cdot (r_\parallel r_\parallel^* - r_\perp r_\perp^*)/(r_\parallel r_\parallel^* + r_\perp r_\perp^*), \tag{15}$$

$$P_u = -\sin 2\sigma_2 \cdot (r_\parallel r_\parallel^* - r_\perp r_\perp^*)/(r_\parallel r_\parallel^* + r_\perp r_\perp^*), \tag{16}$$

where

$$r_\parallel = \frac{n\cos\theta_0 - \cos\theta_t}{n\cos\theta_0 + \cos\theta_t}, \tag{17}$$

$$r_\perp = \frac{\cos\theta_0 - n\cos\theta_t}{\cos\theta_0 + n\cos\theta_t}, \tag{18}$$

and θ_0 is connected with θ_t by Snell's law: $\sin\theta_0 = \mathrm{Re}(n)\sin\theta_t$ where θ_t is the refraction angle in the bare ice. From these equations, each neutral point, for example, can be seen in the measurement angle corresponding to the angle under the condition of $P_q = 0$ and $P_u = 0$ in Eqs. (15) and (16), respectively.

Fig. 7d depicts polar contour plots of P_q and P_u and measured and calculated neutral points at $\lambda = 1630$ nm. The calculated neutral points were roughly consistent with the measured ones. However, there was a difference in the backscattering regions ($\Theta > 150^\circ$).

This could be due to the contribution of the surface roughness in the bare ice. We employed the Fresnel reflection matrix $\mathbf{R}$ in which the surface is an idealized surface that is perfectly smooth. However, the bare ice surface was not perfectly smooth as shown in Fig. 1b. As a result, a moderate polarization was observed in the backscattering regions, showing a difference between the calculations and the measurements.

In the VIS and NIR regions, a weak angular dependence was observed in P_q (except for the forward direction) and P_u. In the forward direction in P_q, the surface reflection did contribute. Since the surface reflection is essentially independent of wavelength, the angular dependence can be seen commonly for all four wavelengths. At other angles except for the forward direction, multiple (volume) scattering would be dominated. Regarding the neutral points, they did not completely match calculated ones based on the surface scattering process. From Fig. 7a–c, the observed neutral points in P_q were shifted to the forward direction and there existed a difference of the neutral points between calculations and measurements. In addition, the neutral points in P_u were quite different

at different wavelengths. Although the reason for the difference is not clear at this moment, this difference could be related to the multiple (volume) scattering, the surface roughness and the illumination conditions that determine the polarization magnitude and the plane of the polarization. Regarding the neutral points in P_u, there is a possibility that these differences are due to the measurement uncertainty since the magnitude of the P_u is rather small at $\lambda = 443$, 673.5 and 868.5 nm. It is desirable to clarify the reason through a quantitative analysis using a radiative transfer model of atmosphere-snow/ice system.

5. Conclusion and closing remarks

Until now, the majority of research into the polarimetric properties of snow and bare ice was concerned with the DoLP. However, each element of the Stokes vector that makes up the measured DoLP was not fully explained yet. In order to understand and quantify polarization properties of snow and bare ice, we carried out spectral measurements of DoLP and its related parameters P_q and P_u in a flat snow/ice field in Hokkaido, Japan. Snow pit works and atmospheric measurements were also conducted at the same time to give an interpretation to the spectral data.

The measurements of polarization in snow and bare ice surfaces demonstrated that the DoLP exhibits unique spectral characteristics. We observed significant signatures associated with the dependence of the DoLP, P_q and P_u on the angular viewing geometry. In addition, an important finding here is that the measurements revealed for the first time the existence of neutral points of P_q and P_u in the snow and bare ice surface. Besides, these unique features appeared to be almost the same regardless of snow/ice condition especially for the NIR and SWIR wavelength. In particular, significant results can be seen in the SWIR regions where the scattering process is dominated by single scattering at the surface layer.

We examined the angular dependence of the neutral points and the signs of P_q and P_u at $\lambda = 1630$ nm. A simple scattering theory revealed that the observed polarization features were related to the measurement geometry (reflection and azimuth angle) regardless of a snow particle size and shape, and ice conditions. In other words, once measurement geometries are determined, the neutral points and the signs of P_q and P_u are determined. Regarding the angular dependence of the DoLP for snow, it was found that it was directly linked to the single scattering properties of snow represented by the scattering phase matrix. For the bare ice, the high DoLP and P_q in the forward direction were mainly a result of the specular reflection at the Brewster angle. At other angles away from Brewster angle, there was less linear polarization due to multiple scattering by ice, air, and scattering/absorbing inclusions in the bare ice. However, the moderate polarization measured in the backscattering regions could be due to the surface roughness of the bare ice. On the other hand, the polarization in the VIS regions was so small but not completely canceled and remained detectable. The angular dependence of the neutral points was somewhat different from that in NIR and SWIR regions, though the overall features were similar each other. These results suggested that the neutral points depend on the polarization magnitude and the plane of polarization that related to the multiple scattering in the atmosphere and snow, and the solar illumination conditions.

The challenge for the future is to develop a forward theoretical model to give a quantitative explanation of the P_q and P_u polarization properties of snow and ice. By coupling these observations with forward/inverse theoretical models, we expect that it will be possible to extract quantitative information regarding snow and ice physical parameters. The SGLI is an imaging sensor onboard GCOM-C satellite, having two polarization channels at $\lambda =$ 673.5 nm and 868.5 nm. The measured polarization features were weak at these channels, but the neutral points were detectable based on the plane of polarization. The polarimetric measurements related to the neutral points are expected to be useful for the retrieval of new snow and ice physical parameters.

In this paper, the polarization properties of DoLP, P_q and P_u were investigated in order to enhance our understanding of light scattering, but those of Q and U themselves were not fully investigated. Furthermore, the polarized reflectance and the angle of linear polarization have not been fully explored yet. It is thus desirable to conduct additional polarimetric measurements for different geometries and wavelengths together with theoretical calculations to interpret optical properties of snow and ice because it is expected to provide the enhanced information compared to that obtained from the DoLP, P_q and P_u alone. These additional measurements are expected to lead a successful polarimetric remote sensing of snow and ice surfaces.

Declaration of Competing Interest

The authors declare that they have no known competing financial interests or personal relationships that could have appeared to influence the work reported in this paper.

CRediT authorship contribution statement

Tomonori Tanikawa: Conceptualization, Methodology, Validation, Formal analysis, Investigation, Writing – original draft, Project administration, Funding acquisition. **Kazuhiko Masuda:** Methodology, Validation, Formal analysis, Writing – review & editing, Visualization. **Hiroshi Ishimoto:** Methodology, Validation, Formal analysis, Writing – review & editing, Visualization. **Teruo Aoki:** Methodology, Investigation, Writing – review & editing, Funding acquisition. **Masahiro Hori:** Investigation, Writing – review & editing. **Masashi Niwano:** Investigation, Writing – review & editing. **Akihiro Hachikubo:** Investigation, Writing – review & editing. **Sumito Matoba:** Investigation, Writing – review & editing. **Konosuke Sugiura:** Investigation, Writing – review & editing. **Takenobu Toyota:** Investigation, Writing – review & editing. **Nozomu Ohkawara:** Methodology, Investigation, Writing – review & editing, Funding acquisition. **Knut Stamnes:** Methodology, Writing – review & editing.

Acknowledgements

We would like to thank M. Igosaki for analysis of snow impurity, and S. Tomioka and K. Fukuhara for logistics support of snow field campaign. This work was conducted as part of the Experimental Research Fund for Global Environment Conservation, the Ministry of the Environment of Japan, Grant Number MLIT1753, the Japan Society for the Promotion of Science, Grants-in-Aid for Scientific Research, Grant Number 16H01772, 17K00534, 18H03363, 20K12142 and 20H00206, the Global Change Observation Mission-Climate (GCOM-C) research project of Japan Aerospace Exploration Agency (JAXA), the Joint Research Program of the Institute of Low Temperature Science, Hokkaido University, Grant Number 20G035 and the Arctic Challenge for Sustainability II (ArCS II), Grant Number JPMXD 1420318865.

Appendix A. The phase and scattering matrices

The phase matrix **M** can be calculated with the scattering matrix **F** and two rotation matrices **L**:

$$\mathbf{M}(\Theta, \sigma_1, \sigma_2) = \mathbf{L}(-\sigma_2)\mathbf{F}(\Theta)\mathbf{L}(\pi - \sigma_1) \tag{A.1}$$

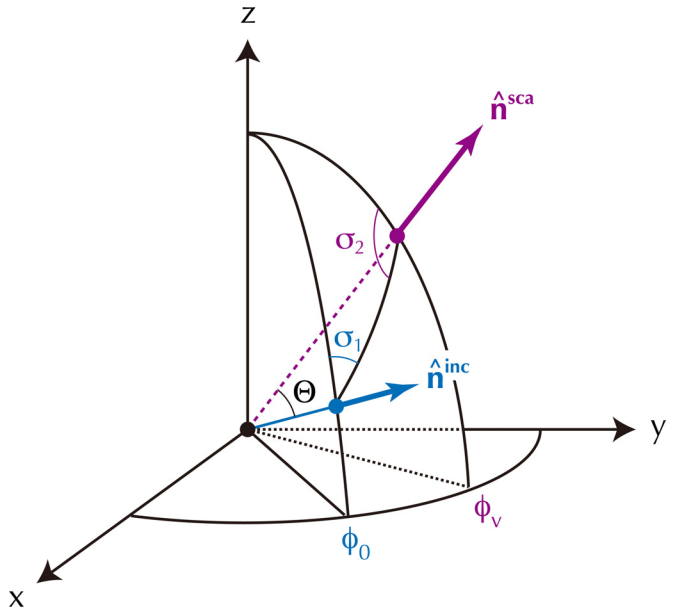

Fig. A.9. Illustration of the relationship between the phase and scattering matrices. This illustration is the same as Fig. 11.3.1 (a) in Mishchenko et al. [33]. $\hat{\mathbf{n}}^{inc}$ and $\hat{\mathbf{n}}^{sca}$ are the direction of incident and scattering waves.

$$= \begin{bmatrix} 1 & 0 & 0 & 0 \\ 0 & \cos 2\sigma_2 & \sin 2\sigma_2 & 0 \\ 0 & -\sin 2\sigma_2 & \cos 2\sigma_2 & 0 \\ 0 & 0 & 0 & 1 \end{bmatrix}$$

$$\times \begin{bmatrix} a_1(\Theta) & b_1(\Theta) & 0 & 0 \\ b_1(\Theta) & a_2(\Theta) & 0 & 0 \\ 0 & 0 & a_3(\Theta) & b_2(\Theta) \\ 0 & 0 & -b_2(\Theta) & a_4(\Theta) \end{bmatrix}$$

$$\times \begin{bmatrix} 1 & 0 & 0 & 0 \\ 0 & \cos 2\sigma_1 & \sin 2\sigma_1 & 0 \\ 0 & -\sin 2\sigma_1 & \cos 2\sigma_1 & 0 \\ 0 & 0 & 0 & 1 \end{bmatrix}$$

where a_i $(i = 1, 2, 3, 4)$ and b_i $(i = 1, 2)$ are elements of normalized scattering matrix, Θ is the scattering angle between incident and scattering angles and σ_1 and σ_2 are angles of rotation that can be calculated from the measurement geometries θ_0, θ_v, ϕ_0 and ϕ_v using spherical trigonometry [33]:

$$\cos\Theta = -\cos\theta_v \cos\theta_0 + \sin\theta_v \sin\theta_0 \cos(\phi_v - \phi_0), \tag{A.2}$$

$$\cos\sigma_1 = \frac{\cos\theta_v + \cos\theta_0 \cos\Theta}{\sin\theta_0 \sin\Theta}, \tag{A.3}$$

$$\cos\sigma_2 = -\frac{\cos\theta_0 + \cos\theta_v \cos\Theta}{\sin\theta_v \sin\Theta}. \tag{A.4}$$

The angles of σ_1 and σ_2 are illustrated in Fig. A.9.

References

[1] Hori M, Sugiura K, Kobayashi K, Aoki T, Tanikawa T, Kuchiki K, et al. A 38-year (1978–2015) northern hemisphere daily snow cover extent product derived using consistent objective criteria from satellite-borne optical sensors. Remote Sens Environ 2017;191:402–18. doi:10.1016/j.rse.2017.01.023.

[2] Henderson GR, Peings Y, Furtado JC. Snow–atmosphere coupling in the Northern Hemisphere. Nat Clim Chang 2018;8:954–63. doi:10.1038/s41558-018-0295-6.

[3] Hammond JC, Saavedra FA, Kampf SK. Global snow zone maps and trends in snow persistence 2001–2016. Int J Climatol 2018;38:4369–83. doi:10.1002/joc.5674.

[4] AMAP. Snow, water, ice and permafrost in the Arctic (SWIPA) 2017. Arctic Monitoring and Assessment Programme (AMAP); 2017. Oslo, Norway. xiv + 269 pp

[5] Shepherd A, Ivins E, Rignot E, Smith B, van den Broeke M, Velicogna I, et al. Mass balance of the greenland ice sheet from 1992 to 2018. Nature 2020;579(7798):233–9. doi:10.1038/s41586-019-1855-2.

[6] Robinson DA, Frei A. Seasonal variability of northern hemisphere snow extent using visible satellite data. Prof Geogr 2000;51:307–14. doi:10.1111/0033-0124.00226.

[7] Flanner M. Arctic climate sensitivity to local black carbon. J Geophys Res 2013;118:1840–51. doi:10.1002/jgrd.50176.

[8] Armstrong RL, Brodzik MJ. Recent Northern Hemisphere snow extent: a comparison of data derived from visible and microwave satellite sensors. Geophys Res Lett 2001;28:3673–6. doi:10.1029/2000GL012556.

[9] Brown RD, Derksen C, Wang L. A multi-data set analysis of variability and changes in Arctic spring snow cover extent, 1967–2008. J Geophys Res 2010;115. doi:10.1029/2010JD013975. D16111

[10] Nolin AW, Dozier J. A hyperspectral method for remotely sensing the grain size of snow. Remote Sens Environ 2000;74:207–16. doi:10.1016/S0034-4257(00)00111-5.

[11] Li W, Stamnes K, Chen B. Snow grain size retrieved from near-infrared radiances at multiple wavelengths. Geophys Res Lett 2001;28(9) 1,699–1,702. doi:10.1029/2000GL011641.

[12] Tanikawa T, Aoki T, Nishio F. Remote sensing of snow grain size and snow impurities from airborne multispectral scanner data using a snow bidirectional reflectance distribution function model. Ann Glaciol 2002;34:74–80. doi:10.3189/172756402781817437.

[13] Stamnes K, Li W, Eide H, Aoki T, Hori M, Storvold R. ADEOS-II/GLI snow/ice products: Part I - scientific basis. Remote Sens Environ 2007;111:258–73. doi:10.1016/j.rse.2007.03.023.

[14] Aoki T, Hori M, Motoyohi H, Tanikawa T, Hachikubo A, Sugiura K, et al. ADEOS-II/GLI snow/ice products: Part II - validation results using GLI and MODIS data. Remote Sens Environ 2007;111:274–90. doi:10.1016/j.rse.2007.02.035.

[15] Hori M, Aoki T, Stamnes K, Li W. ADEOS-II/GLI snow/ice products: Part III - retrieved results. Remote Sens Environ 2007;111:291–336. doi:10.1016/j.rse.2007.01.025.

[16] Scambos T, Haran T, Fahnestock M, Painter TH, Bohlander J. MODIS-based mosaic of Antarctica (MOA) data sets: continent-wide surface morphology and snow grain size. Remote Sens Environ 2007;111(2–3):242–57. doi:10.1016/j.rse.2006.12.020.

[17] Jin Z, Charlock TP, Yang P, Xie Y, Miller W. Snow optical properties for different particle shapes with application to snow grain size retrieval and MODIS/CERES radiance comparison over Antarctica. Remote Sens Environ 2008;112:3563–81. doi:10.1016/j.rse.2008.04.011.

[18] Lyapustin A, Tedesco M, Wang Y, Aoki T, Hori M, Kokhanovsky AA. Retrieval of snow grain size over Greenland from MODIS. Remote Sens Environ 2009;113:1976–87. doi:10.1016/j.rse.2009.05.008.

[19] Zege EP, Katsev IL, Malinka AV, Prikhach AS, Heygster G, Wiebe H. Algorithm for retrieval of the effective snow grain size and pollution amount from satellite measurements. Remote Sens Environ 2011;115(10):2674–85. doi:10.1016/j.rse.2011.06.001.

[20] Wiebe H, Heygster G, Zege E, Aoki T, Hori M. Snow grain size retrieval SGSP from optical satellite data: validation with ground measurements and detection of snow fall events. Remote Sens Environ 2013;128(21):11–20. doi:10.1016/j.rse.2012.09.007.

[21] Chen N, Li W, Fan Y, Zhou Y, Aoki T, Tanikawa T, et al. Snow parameter retrieval (SPR) algorithm for GCOM-C/SGLI. Remote Sens Environ 2021. (under review)

[22] Wiscombe WJ, Warren SG. A model for the spectral albedo of snow. I: pure snow. J Atmos Sci 1980;37(12):2712–33. doi:10.1175/1520-0469(1980)037⟨2712:AMFTSA⟩2.0.CO;2.

[23] Warren SG, Wiscombe WJ. A model for the spectral albedo of snow. II: snow containing atmospheric aerosols. J Atmos Sci 1980;37(12):2734–45. doi:10.1175/1520-0469(1980)037⟨2734:AMFTSA⟩2.0.CO;2.

[24] Grenfell TC, Warren SG. Representation of a nonspherical ice particle by a collection of independent spheres for scattering and absorption of radiation. J Geophys Res 1999;104(D24):31697–709. doi:10.1029/1999JD900496.

[25] Aoki T, Aoki T, Fukabori M, Hachikubo A, Tachibana Y, Nishio F. Effects of snow physical parameters on spectral albedo and bi-directional reflectance of snow surface. J Geophys Res 2000;105(D8):10219–36. doi:10.1029/1999JD901122.

[26] Painter TH, Dozier J. Measurements of the hemispherical-directional reflectance of snow at fine spectral and angular resolution. J Geophys Res 2004;109. doi:10.1029/2003JD004458. D18115

[27] Tanikawa T, Aoki T, Hori M, Hachikubo A, Abe O, Aniya M. Monte Carlo simulations of spectral albedo for artificial snowpacks composed of spherical and nonspherical particles. Appl Opt 2006;45(21):5310–19. doi:10.1364/AO.45.005310.

[28] Marks A, Fragiacomo C, MacArthur A, Zibordi G, Fox N, King MD. Characterisation of the HDRF (as a proxy for BRDF) of snow surfaces at Dome C, Antarctica, for the inter-calibration and inter-comparison of satellite optical data. Remote Sens Environ 2015;158:407–16. doi:10.1016/j.rse.2014.11.013.

[29] Kokhanovsky A, Lamare M, Mauro BD, Picard G, Arnaud L, Dumont M, et al. On the reflectance spectroscopy of snow. Cryosphere 2018;12:2371–82. doi:10.5194/tc-12-2371-2018.

[30] Tanikawa T, Kuchiki K, Aoki T, Ishimoto H, Hachikubo A, Niwano M, et al. Effects of snow grain shape and mixing state of snow impurity on retrieval of snow physical parameters from ground-based optical instrument. J Geophys Res 2020;125 e2019JD031858. doi:10.1029/2019JD031858.
[31] Hansen JE, Travis LD. Light scattering in planetary atmosphere. Space Sci Rev 1974;16:527–610. doi:10.1007/BF00168069.
[32] Talmage DA, Curran PJ. Remote sensing using partially polarized light. Int J Remote Sens 1986;7:47–64. doi:10.1080/01431168608954660.
[33] Mishchenko MI, Travis LD, Lacis AA. Multiple scattering of light by particles: radiative transfer and coherent backscattering. Cambridge University Press; 2006.
[34] Deschamps P, Breon F, Leroy M, Podaire A, Bricaud A, Buriez J, et al. The polder mission: instrument characteristics and scientific objectives. IEEE Trans Geosci Remote Sens 1994;32(3):598–615. doi:10.1109/36.297978.
[35] Bréon FM, Goloub P. Cloud droplet effective radius from spaceborne polarization measurements. Geophys Res Lett 1998;25:1879–82. doi:10.1029/98GL01221.
[36] Deuzé JL, Goloub P, Herman M, Marchand A, Perry G, Susana S, et al. Estimate of the aerosol properties over the ocean with POLDER. J Geophys Res 2000;105:15329–46. doi:10.1029/2000JD900148.
[37] Cairns B, Russell EE, LaVeigne JD, Tennant PMW. Research scanning polarimeter and airborne usage for remote sensing of aerosols. Proc SPIE 5158, polarization science and remote sensing; 2003. doi:101117/12518320.
[38] Ottaviani M, van Diedenhoven B, Cairns B. Photopolarimetric retrievals of snow properties. Cryosphere 2015;9:1933–42. doi:10.5194/tc-9-1933-2015.
[39] Goloub P, Herman M, Deuze JL. Contrast between polarization properties of snow/ice and clouds. Antarctic J United States 1992;27:199–202.
[40] Leroux C, Deuzé J, Goloub P, Sergent C, Fily M. Ground measurements of the polarized bidirectional reflectance of snow in the near-infrared spectral domain: comparisons with model results. J Geophys Res 1998;103(D16) 19,721–19,731. doi:10.1029/98JD01146.
[41] Perovich DK. Observation of the polarization of light reflected from sea ice. J Geophys Res 1998;103(C3):5563–75. doi:10.1029/97JC01615.
[42] Tanikawa T, Hori M, Aoki T, Hachikubo A, Kuchiki K, Niwano M, et al. In situ measurements of polarization properties of snow surface under the Brewster geometry in Hokkaido, Japan, and northwest Greenland ice sheet. J Geophys Res 2014;119:13946–64. doi:10.1002/2014JD022325.
[43] Peltoniemi J. Spectropolarised ray-tracing simulations in densely packed particulate medium. J Quant Spectrosc RadiatTransf 2007;108(2):180–96. doi:10.1016/j.jqsrt.2007.05.009.
[44] Lv Y, Sun Z. The reflectance and negative polarization of light scattered from snow surface with different grain size in backward direction. J Quant Spectrosc RadiatTransf 2014;113:472–81. doi:10.1016/j.jqsrt.2013.09.010.
[45] Peltoniemi J, Hakala T, Suomalainen J, Puttonen E. Polarised bidirectional reflectance factor measurements from soil, stones, and snow. J Quant Spectrosc RadiatTransf 2009;110:1940–53. doi:10.1016/j.jqsrt.2009.04.008.
[46] Sun Z, Zhao Y. The effects of grain size on bidirectional polarized reflectance factor measurements of snow. J Quant Spectrosc RadiatTransf 2011;112:2372–83. doi:10.1016/j.jqsrt.2011.05.011.
[47] Sun W, Wielicki BA, Baize RR, Lukashin C, Hu Y, Zubko E, et al. Modeling polarized solar radiation from a snow surface for correction of polarization-induced error in satellite data. J Quant Spectrosc RadiatTransf 2019;222–223:154–69. doi:10.1016/j.jqsrt.2018.10.011.
[48] Hovenier JW, van der Mee CVM. Fundamental relationships relevant to the transfer of polarized light in a scattering atmosphere. Astron Astrophys 1983;196:287–95.
[49] Radiative transfer in coupled environmental systems. Stamnes K, Stamnes J, editors. Wiley-VCH; 2015.
[50] Suomalainen J, Hakala T, Peltoniemi J, Puttonen E. Polarised multiangular reflectance measurements using the finnish geodetic institute field goniospectrometer. Sensors 2009;9:3891–907. doi:10.3390/s90503891.
[51] Fierz C, Armstrong RL, Durand Y, Etchevers P, Greene E, McClung DM, et al. The international classification for seasonal snow on the ground Tech. Rep.. IHP-VII Technical Documents in Hydrology No 83, IACS Contribution No1, UNESCO-IHP, Paris, 90pp; 2009.
[52] Tanikawa T, Aoki T, Hori M, Hachikubo A, Aniya M. Snow bidirectional reflectance model using non-spherical snow particles and its validation with field measurements. EARSeL eProceedings 2006;5(2):137–45.
[53] Aoki T, Hachikubo A, Hori M. Effects of snow physical parameters on shortwave broadband albedos. J Geophys Res 2003;108(D19). doi:10.1029/2003JD003506.
[54] Chow JC, Watson JG, Pritchett LC, Pierson WR, Frazier CA, Purcell RG. The DRI thermal/optical reflectance carbon analysis system: description, evaluation and applications in u.s. air quality studies. Atmos Environ 1993;27:1185–201. doi:10.1016/0960-1686(93)90245-T.
[55] Kuchiki K, Aoki T, Niwano M, Matoba S, Kodama Y, Adachi K. Elemental carbon, organic carbon, and dust concentrations in snow measured with thermal optical and gravimetric methods: variations during the 2007–2013 winters at Sapporo, Japan. J Geophys Res 2015;120:868–82. doi:10.1002/2014JD022144.
[56] Warren SG, Brandt RE. Optical constants of ice from the ultraviolet to the microwave: a revised compilation. J Geophys Res 2008;113. doi:10.1029/2007JD009744. D14220
[57] Imaoka K, Kachi M, Fujii H, Murakami H, Hori M, Ono A, et al. Global change observation mission (GCOM) for monitoring carbon, water cycles, and climate change. Proc IEEE 2010;98:717–34. doi:10.1109/JPROC.2009.2036869.
[58] Mishchenko MI, Travis LD, Lacis AA. Scattering, absorption, and emission of light by small particles. Cambridge University Press; 2002.
[59] Masuda K, Ishimoto H, Mano Y. Efficient method of computing a geometric optics integral for light scattering by nonspherical particles. Pap Meteorol Geophys 2012;63:15–19. doi:10.2467/mripapers.63.15.
[60] Ishimoto H, Adachi S, Yamaguchi S, Tanikawa T, Aoki T, Masuda K. Snow particles extracted from X-ray computed microtomography imagery and their single-scattering properties. J Quant Spectrosc RadiatTransf 2018;209:113–28. doi:10.1016/j.jqsrt.2018.01.021.
[61] Takashima T, Masuda K. Degree of radiance and polarization of the upwelling radiation from an atmosphere-ocean system. Appl Opt 1985;24(15):2423–9. doi:10.1364/AO.24.002423.